Site Requirements for Inhibition-free CO Oxidation over Silica-supported Bimetallic PdCu Alloys

Stephen Thomas Kristy[1,2], Scott Svadlenak[1], Adam S. Hoffmann[2], Simon R. Bare[2], Konstantinos A. Goulas[1]*

1. School of Chemical, Biological and Environmental Engineering, Oregon State University, Corvallis, OR 97331
2. Stanford Synchrotron Radiation Lightsource, SLAC National Accelerator Laboratory, Menlo Park, CA 94025

Abstract:

Pd catalysts are highly active for CO oxidation but suffer from inhibition by NO at low temperatures (< 150 °C). We posit that incorporation of Cu into the Pd catalyst will improve low-temperature CO oxidation activity and reduce inhibition from competitive adsorbers. To probe this hypothesis, a series of PdCu alloys with different Pd:Cu ratios were synthesized and tested in the temperature-programmed oxidation of CO in the presence and absence of NO. Incorporation of small amounts of Cu into Pd improves the reactivity, as well as the resistance to NO inhibition. Beyond this, Cu incorporation into the Pd has a detrimental effect on the activity for CO oxidation. Based on combined infrared and X-ray absorption spectroscopy studies, we show that high activity and resistance to inhibition requires alloying of Pd and Cu and the formation of a diverse surface, while surface segregation of Cu results in poor activity and inhibition.

Keywords: CO oxidation, Surface Diversity, DRIFTS, XAS, Diesel Oxidation Catalysts

1. Introduction

Diesel engines can reach much higher thermal efficiency compared to gasoline engines and are broadly used in heavy duty vehicles, and to a lesser extent in marine, stationary and personal vehicle applications[1]. Key to the higher efficiency is their lean operation, which, however, comes with a penalty of higher emissions, particularly of NOx and particulate matter.[2] Untreated diesel emissions are carcinogenic and contribute to respiratory health problems in urban environments.[3] To address this issue, the exhaust gas of diesel engines is treated over a series of plug flow catalytic reactors and filters to either remove or convert toxic species into inert ones.[4,5] In such a system, the diesel oxidation catalyst (DOC) is usually the first reactor inline, which serves the purpose of oxidizing the species that pass through. The primary target species of the DOC is CO, which oxidizes to CO_2 during successful after-treatment. Nitric oxide and various hydrocarbons will also be partially or fully oxidized.[6]

DOCs are typically Pt and Pd and their alloys supported on various oxide supports.[7–13] Pt is highly active for the above reactions, while the addition of Pd increases the catalysts' resistance to sintering in addition to facilitating oxidation.[11,14] Standard diesel vehicles normally operate at 327 °C. Under the reagent concentrations present in standard diesel exhaust conventional DOCs are 100% effective for CO oxidation at 190 °C.[15] Therefore, there is a period from start up until the exhaust reaches a temperature of 190 °C where the DOC is ineffective, causing unconverted emissions. Low temperature combustion (LTC) diesel engines exhibit high fuel efficiency due to lean combustion conditions but contain higher CO content than standard conventional diesel engines. Reactivity Controlled Compressed Ignition (RCCI) LTC engines operate at about 152 °C and use a combination of fuel sources to achieve high efficiency. However, they have four times more hydrocarbons and ten times more CO in their exhaust. At these high concentrations, conventional DOCs are not 100% effective until 300 °C.[15] The low temperature activity is a direct result of poisoning, or blocking of the surface-active sites, by reagents strongly bonded to the surface.[14] This presents an opportunity to design oxidation catalysts with lower temperature activity for enhanced low temperature emission abatement.

Song and Grabow[16] performed descriptor based microkinetic model simulations combined with density functional theory (DFT) to computationally screen metal catalysts for low temperature CO oxidation. The results of the model are consistent with the observed high activity of Pd:Pt

alloys under standard diesel conditions (327 °C, low CO concentration). The model also predicts poor activity at lower temperature and higher CO concentration (LTC conditions). The results of the screening indicate no single metal effectively oxidizes CO under LTC conditions. Therefore, the authors investigated alloys of transitions metals and determined that bimetallic alloys of platinum group metals (PGMs – Pd and Pt) and coinage metals (Cu, Ag) should offer lower temperature activation for CO oxidation under LTC conditions, with NO present.

In our recentwork,[17,18] we demonstrated experimentally that PdCu catalysts outperform their monometallic Pd counterparts, in terms of both CO oxidation activity and NO inhibition. We attributed these effects to the electronic exchange of Cu and Pd, as well as the mobility of Cu from the bulk to the surface upon light-off, which offers a binding site for O_2 to adsorb and react.

However, missing from this interpretation is a conclusive determination of the active site requirements for inhibition-free oxidation. Our working hypothesis is that that alloying enables the formation of diverse Pd-Cu ensembles at the surface of the catalyst, thereby restricting poisoning by CO, NO and HC to PGM sites, as opposed to the entire surface. The geometric arrangements of unique active sites on the surface in alloys offer promotional spatial distribution of adsorbates, Therefore, the surface with a ratio of Pd and Cu closest to unity have the highest activity. To probe this hypothesis, we synthesized a set of silica-supported PdCu catalysts with Pd:Cu ratios equal to 3:1, 1:3 and 1:1, along with a monometallic control Pd catalyst. The catalyst with the highest CO oxidation activity is a 3:1 Pd:Cu alloy, which also demonstrates no inhibition by NO. Diffuse reflectance infrared Fourier transform spectroscopy (DRIFTS) and X-ray absorption spectroscopy (XAS) studies reveal that the higher incorporation of Cu likely leads to a detrimental effect by covering up the active Pd surface exclusively, rather than by creating a surface diverse in PdCu ensembles.

2. Materials and Methods

Catalyst Synthesis: We synthesized a monometallic Pd and alloyed PdCu catalyst with a 3:1, 1:1, and 1:3 Pd:Cu atomic ratio. We used the strong electrostatic adsorption (SEA) method reported by Regalbuto and coworkers.[19–22] The weight loading used for synthesis is listed in Table S1. For the synthesis, 5 g of silica gel (Davisil 636, Millipore Sigma) were mixed with 45 mL of deionized water (18.2 Ω) and 4 mL of stock ammonium hydroxide solution (18 mole/L). The palladium nitrate and copper nitrate precursor (TCI America) were dissolved in 5 mL of

water, to which 4 mL of stock ammonium hydroxide solution were added. The solution of metal ammine nitrate precursors was added to silica under vigorous stirring. The mixture was stirred for 1 h and the solids separated from the liquid by vacuum filtration. The retentate was washed with 100 mL of water and then dried under ambient air pressure at 90 ˚C for 16 h. Portions of the dried solids were then treated for 4 h under flowing air (100 mL $min^{-1}g^{-1}$) in a tubular furnace at 700 ˚C with a heating rate of 5 ˚C min^{-1}.

Catalyst Characterization:

Electron Microscopy: Samples were prepared for transmission electron microscopy (TEM) imaging by grinding them with a mortar and pestle, suspending the samples in ethanol and sonicating them for 15 min. They were then deposited on carbon type B 300 mesh Cu grids (Ted Pella). TEM analysis was performed on a FEI TITAN 80-200 TEM/STEM microscope. Samples were imaged at 200 kV with a typical magnification of 200 – 300 kx. The average particle diameter was determined from greater than 100 imaged particles. Particle size distribution for the four catalysts is shown in Figure S1.

Chemical maps of Pd and Cu were obtained utilizing a Titan FEI microscope equipped with chemiSTEM technology which is equipped with Energy Dispersive X-ray Spectroscopy (EDX) capabilities. Formvar/carbon on 200 mesh gold TEM grids were obtained from Ted Pella and were used for the chemical mapping. Chemical maps were collected with a spot size of 0.2 nm, a voltage setting of 200 kV, and a 1 nm EDX excitation volume. The condenser aperture was set to 100.

DRIFTS: DRIFTS measurements were performed using a Thermo Nicolet 6700 FTIR spectrometer, equipped with a Harrick DRIFTS cell. A liquid nitrogen-cooled Mercury Cadmium Telluride (MCT) detector was used for data acquisition and the native OPUS software for data processing. A gas manifold with mass flow controllers was used to deliver gases (H_2, 10% CO/He) to the Harrick cell and the outlet gaseous species were analyzed with a Hiden QGA mass spectrometer. In all experiments, 20 mg of undiluted catalyst was crushed, and loaded onto a bed of ~20 mg γ-Al_2O_3 within the DRIFTS cell. Before experiments catalysts were reduced in H_2 at 250 °C for 45 minutes (20 cm^3 min^{-1}, 60 L g^{-1} h^{-1} space velocity). The cool, post reduction catalyst is used as the background in all experiments. In temperature-programmed desorption (TPD) experiments, 10% CO (balance He) was fed at 20 cm^3 min^{-1} for 15 minutes at room

temperature and then purged for 15 minutes with He. In TPD experiments 10 °C min^{-1} heating ramp rates were used up to 240 °C. DRIFTS spectra were recorded at 4 cm^{-1} resolution with 30 scans merged to generate one spectrum with improved signal-to-noise. Redhead's method was used to determine coverage by calculating the integral of the area under the CO binding peak locations present in FTIR spectra.[23] The largest acquired peak is normalized to 1 for each unique peaks in each spectrum. All peaks were fit using Gaussian, Lorentzian, or Voigt fitting functions to determine the appropriate number of peaks under each spectral peak and the area under each peak. A full analysis of peak fitting is included in the SI.

X-ray Absorption Spectroscopy: X-ray absorption spectroscopy (XAS) data were recorded at beamline 9-3 at the Stanford Synchrotron Radiation Lightsource using a liquid nitrogen cooled double Si(220) (φ=0°) crystal monochromator with Rh-coated collimating and focusing mirrors for harmonic rejection. X-ray absorption near edge structure (XANES) and extended X-ray absorption fine structure (EXAFS) spectra were collected at the Cu (8979.0 eV) and (24350.0 eV) Pd K-edges in fluorescence mode using a PIPS diode. A reference spectrum of a Cu or Pd foil was collected in transmission mode simultaneously, using N_2 or Ar-filled ion chambers, respectively, for energy calibration and spectra alignment.

As prepared catalyst and post reduction catalyst were probed with XAS. Crushed, undiluted catalyst powders were loaded into a 3 mm polyimide tube ("Kapton", 3mm diameter) plug flow reactor.[24,25] As prepared data was collected following loading into the reactor. The reduction procedure follows the same process described in the activity testing section below (20 cm^3 min^{-1}, 60 L g^{-1} h^{-1}). Post reduction data was collected on the cool, He-purged reactor following reduction using step scans. Data preprocessing and fitting were performed in the Demeter suite[26]. Cu K-edge XAS data were calibrated to 8979.0 eV by defining the edge as the location of the maximum in the first derivative of xμ(E), while Pd K-edge data were calibrated to 24350.0 eV (maximum of the first derivative of xμ(E)). All data were aligned using metal foil standards that were measured as references simultaneously with the samples. Linear combination fitting (LCF) was performed on the as-prepared catalyst samples to compare bulk oxide and bulk metal features using PdO, CuO, and Cu_2O reference foils. EXAFS fits were performed using a variety of *k*-range and a *R*-range values, between 1.5-13.5 $Å^{-1}$ and 1-3 Å, respectively. Scattering paths were acquired from Materials Explorer, part of the Materials Project.[27] The paths were

downloaded as Pd and edited to contain a Pd-Cu path. The amplitude reduction factor (S_0^2) is 0.87 for Pd fits, as determined by a fit to the Pd foil. PdO, CuO, and Cu_2O reference spectra were provided by the Co-ACCESS team at SSRL for XAS analysis. For Cu, S_0^2 is 0.80 as determined by a fit to the Cu foil. All fits for catalyst foils, as prepared catalyst, TPRs, and other experimental details are included in the XAS section of the SI.

ICP-OES: Approximately 10 mg of individual catalyst sample were weighed into acid-cleaned 30ml Teflon beakers, to which ~3 ml of 3:1 concentrated HF:concentrated HNO_3 solution was added. The beakers were sealed and heated overnight at 150 ºC. The resulting sample solutions were evaporated to dryness and then redigested in 3 ml concentrated HNO_3 overnight at 150 ºC. Subsequently, sample solutions were again evaporated to dryness and dissolved in 10 mL of an aqueous HNO_3 (3.7 M) and HCl (0.5 M) solution. Digested sample solutions were allowed to cool and thermally equilibrate prior to being weighed.

Analyses were completed using a Spectros Arcos II ICP-OES in end-on configuration. Cu was analyzed at 324.754 nm and Pd was analyzed utilizing 340.458 nm. A matrix matched acid blank plus six standard solutions were prepared for calibration. 0.5ml digested sample was combined with 4.5ml matrix matched solution for analysis (in-run dilution factor of 10). Argon measured at 430.010 was utilized as a monitor line to verify no significant plasma suppression occurred between standards and samples.

Catalyst Activity Testing: We performed multi component oxidation experiments on the four synthesized catalysts using a plug flow reactor which holds catalyst and allows reagent and product gases to flow to a Fourier Transform Infrared Spectroscopy (FTIR – California Analytical Instrument 600 FTIR (SC)) gas cell, which measures outlet concentrations. In all experiments, the catalyst was diluted 1:1000 with silica gel (Davisil Grade 635 Silica gel, pore size 60 Å, 60-100 mesh – Millipore Sigma) by repeated crushing and pelletizing processes, sieved to eliminate particles smaller than 106 μm, and loaded into the glass reactor directly on top of the porous frit in the reactor chamber. Since the four catalysts have different metal loadings, the dispersion based on TEM measured particle size was used to load equal surface moles of each catalyst.

A gas manifold with electronic mass flow controllers is used to deliver reactant gases to the reactor, and the effluent is analyzed by FTIR. Reactive gases were obtained from Airgas (2%

O_2/Ar, 20% CO/He, 200 ppm NO/N_2). Hydrogen was generated in the laboratory by a Parker hydrogen generator. In a typical experiment, the gas phase within the reactor was comprised of 0.5 kPa CO, 1.5 kPa O2 and, when required, 50 ppm NO.

The fresh (as prepared) catalyst is reduced with pure H_2 flowing at 20 cm^3 min^{-1} while being heated at 6 ˚C min^{-1} from room temperature (RT) to 250 ˚C and held for 45 min before cooling to RT. The first temperature programmed oxidation experiment, CO (0.5 kPa) and O_2 (1.5 kPa) in inert gas are introduced over the catalyst. Table S1 displays the catalyst powder masses loaded and the space velocity for each catalyst testing during these activity tests. The system is heated at a ramp rate of 2 ˚C min^{-1} from 25 ˚C until several scans at 100% conversion are acquired. The system is then cooled to RT and reduced again under the TPR conditions and cooled to RT. The second TPO follows the same procedure as the first with the addition of the 200 ppm NO feed. After complete oxidation of CO, the system is cooled to room temperature, and re-reduced a final time and subjected to the conditions of the first TPO. This process of heating and cooling during reduction and oxidation conditions is illustrated in Figure S2. The purpose of this series of three reductions and oxidations is to use the average of the 1st and 3rd TPO runs to eliminate deactivation effects in the comparison of CO single oxidation with NO/CO co-oxidation. Conversion data were all set to be zero at 50 °C in plot below. A 20-point rolling average, corresponding to 5 seconds, was applied to conversion data to reduce noise.

3. Results and discussion

TEM: The results of the TEM analysis of the average nanoparticle sizes are presented in Table S1 and Figure S1. Figure 1 also displays representative TEM images from each sample. The measured average particle sizes are 2.9, 3.1, 3.7 and 3.4 nm for the Pd, 3:1, 1:1, and 1:3 Pd:Cu samples, respectively.

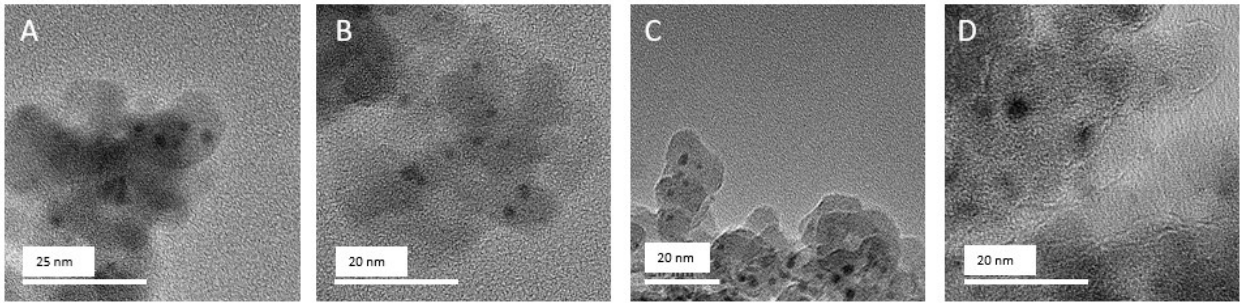

Figure 1: Representative TEM images for (A) Pd, (B) 3:1 PdCu, (C) 1:1 PdCu, (D) 1:3 PdCu. Note the difference in scale for A. The darker areas are the metallic nanoparticles.

Catalyst Activity: Figure 2 shows representative light off activity curves for the CO TPO for the Pd and PdCu catalysts during CO oxidation (A), and during CO oxidation when NO is introduced as a competitive reagent (B). During CO oxidation, there is a clear trend of decreasing activity with increasing Cu content. The Pd catalyst shows severe inhibition when 50 ppm NO is added to the reagent streams (Figure 2B), whereas the 3:1 PdCu shows little inhibition. The 1:1 and 1:3 catalysts show poorer activity for both CO oxidation and are also inhibited with the presence of NO.

Figure 3 displays the T_{50}, the temperature at 50% conversion, for all catalysts tested. The T_{50} values are often used in the context of emission control catalysis to compare catalysts in a regime of few mass and heat transfer artifacts and to simulate the startup of a vehicle.[28–32] The data in Figures 2 and 3 show that, of the catalysts tested, the 3:1 PdCu catalyst is the optimal material for low temperature CO oxidation, both with and without NO present. Moreover, the 3:1 PdCu shows minimal inhibition upon introduction of NO, whereas the Pd is inhibited by 18 °C (note the spread in the T_{50} between the data markers in Figure 3). Some deactivation is observed for the 1:1 PdCu after each run, and, while 1:3 PdCu shows severe NO inhibition, it recovers its activity in the third run.

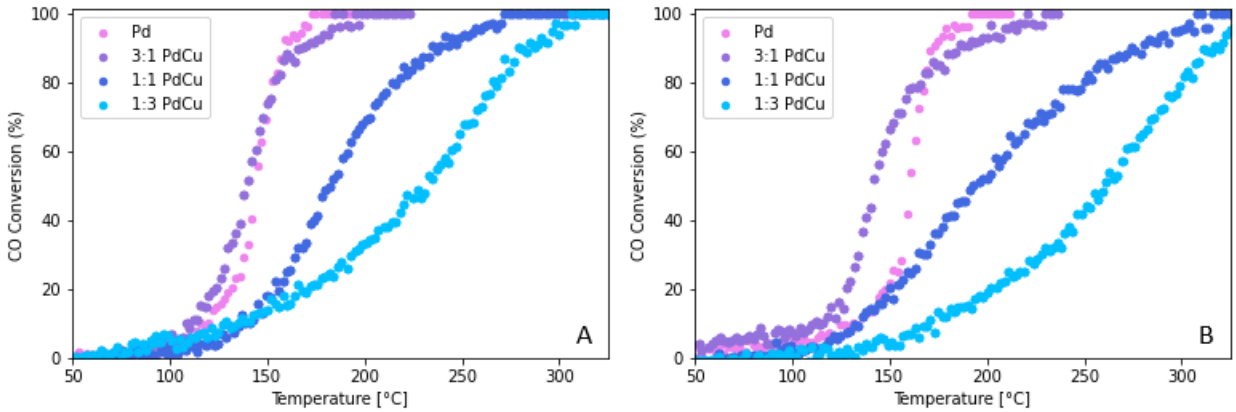

Figure 2: CO conversion as a function of temperature over the four synthesized catalysts. (A) is CO oxidation, (B) is CO and NO co-oxidation. Conversion is measured as a percentage of CO via inline FTIR, and temperature represents reactor temperature. Total Pressure: 101.325 kPa, O_2 partial pressure: 1.5 kPa, CO partial pressure: 0.5 kPa. 2 °C min^{-1} heating rate. Space Velocity: Pd - (990 L g^{-1} h^{-1}), 3:1–PdCu - (832 L g^{-1} h^{-1}), 1:1–PdCu - (2080 L g^{-1} h^{-1}), 1:3–PdCu - (1109 L g^{-1} h^{-1}).

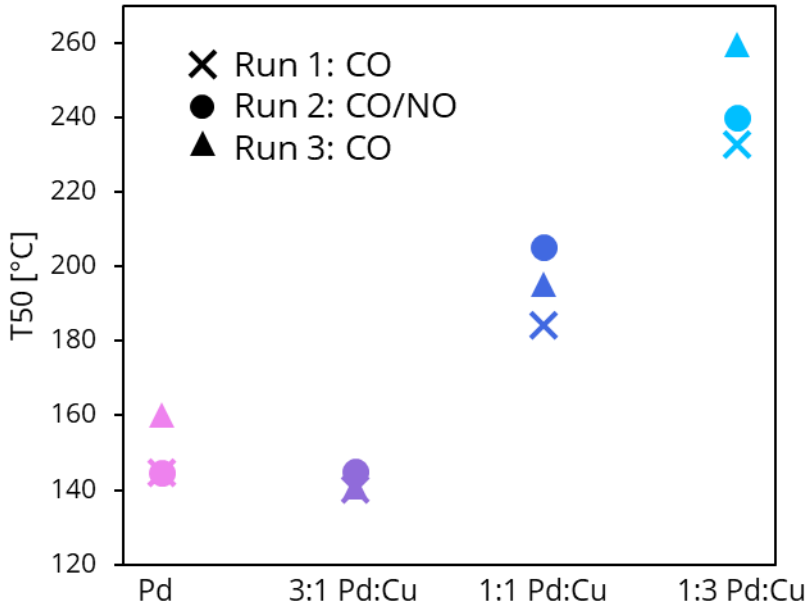

Figure 3: T50, or temperature at 50% CO conversion over the series of catalyst tested. Conversion is measured as a percentage of CO via inline FTIR, and temperature represents reactor temperature. Total Pressure: 101.325 kPa, O_2 partial pressure: 1.5 kPa, CO partial pressure: 0.5 kPa. 2 °C min^{-1} heating rate. Space Velocity: Pd - (990 L g^{-1} h^{-1}), 3:1–PdCu - (832 L g^{-1} h^{-1}), 1:1–PdCu - (2080 L g^{-1} h^{-1}), 1:3–PdCu - (1109 L g^{-1} h^{-1}).

Both Pd and 3:1 PdCu show high activity at low temperatures (150 °C) for CO oxidation.

However, Pd activity is inhibited by the presence of 50 ppm NO, whereas 3:1 PdCu shows

resistance to inhibition. Somewhat surprisingly, the samples with 1:1 and 1:3 Pd:Cu ratios show significantly diminished activity, combined with NO-induced inhibition. To probe the reasons for this activity loss, we use spectroscopy to understand the effects of the alloying ratio on the surface and bulk structure of the catalyst, and, in doing so, ascertain the site requirements for the uninhibited oxidation reaction.

Infrared Spectroscopy: FTIR of chemisorbed CO using DRIFTS TPD experiments was conducted to help understand how Cu incorporation affects the surface of the nanoparticles under CO saturation and desorption conditions. The ambient temperature scans for each material are shown in Figure 4 and used to identify the various CO binding configurations. (The unstacked spectra comparison is found in Figure S3).

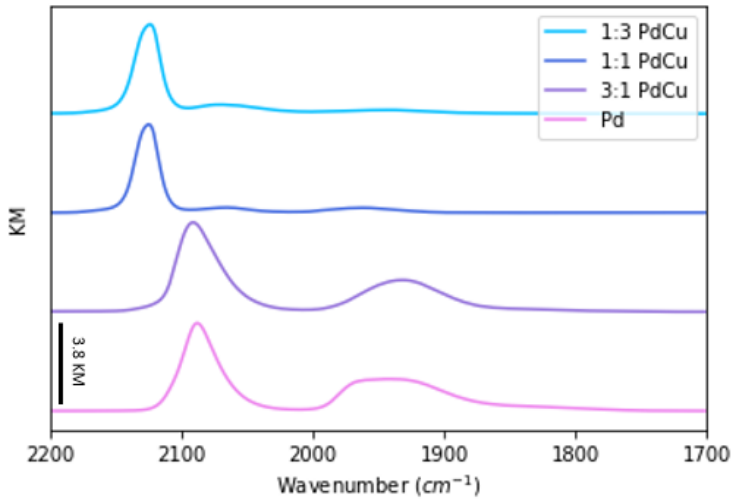

Figure 4: - CO DRIFTS spectra of PdCu catalysts at ambient temperature.

The peak at 2130 cm^{-1} in the 1:1 and 1:3 PdCu is attributed to CO bound to surface Cu.[33] The peak at 2087 cm^{-1} in Pd and 2090 cm^{-1} in 3:1 PdCu are CO linearly bound atop a Pd atom.[34] This linear CO peak is also apparent in the other alloys, but smaller in magnitude (Figure S2). Between 1900 and 2000 cm^{-1} there is a peak attributed to bridge-bound CO between two Pd atoms. The peak appears in different locations and is significantly broader in the case of the Pd catalyst. This is likely the result of the different bridge-binding configurations over Pd due to the presence of different sets of facets.[35] For example, when comparing the position of the bridge-bound CO in Pd versus 3:1 PdCu, it is clear that the peak in Pd is wider at the crest. Additionally,

the apex of the bridging peak in 1:1 and 1:3 PdCu appear to be at different wavenumber values. These are indicators that there is diversity in the types of Pd atoms available for binding under these conditions between the four materials, such as different faceted bridge sites.[18]

Figure 5 shows the evolution of the spectra for the TPD experiments on all materials. The vibrational peaks due to CO bound to both Cu and Pd decreases on all initial sites with increasing temperature, as expected. However, all four sets of spectra show an increase in the to CO-Pd hollow site vibrational peak due (between 1750 and 1850 cm^{-1}), with more pronounced growth in Pd and 3:1 PdCu.

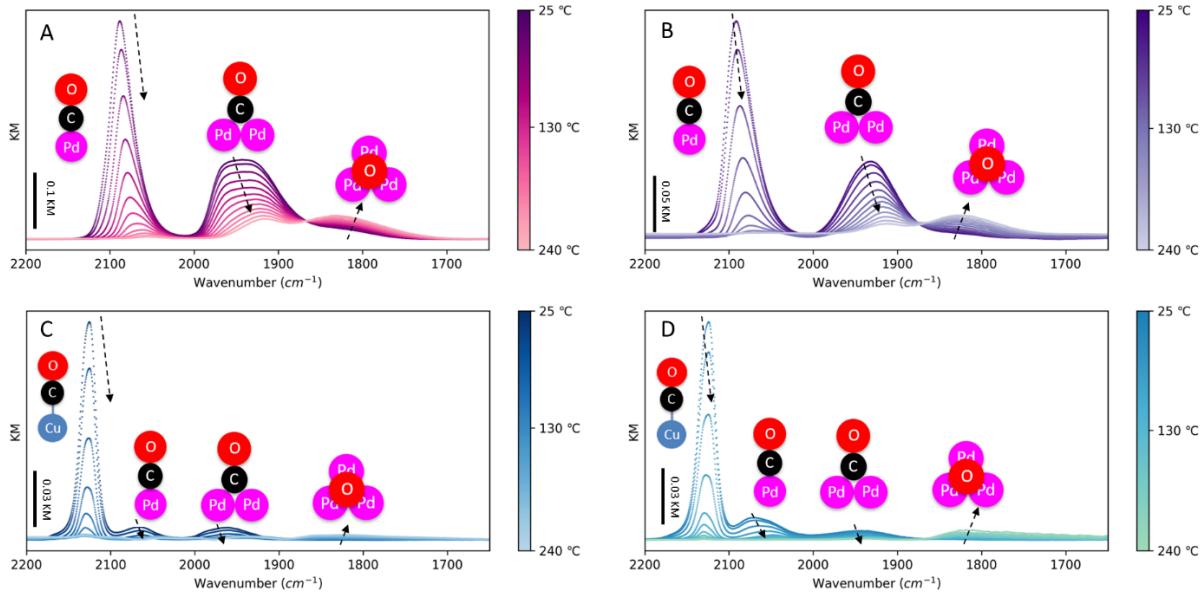

Figure 5: CO TPD DRIFTS as a function of temperature (10 °C min^{-1} ramp). (A) Pd, (B) 3:1 PdCu, (C) 1:1 PdCu, and (D) 1:3 PdCu spectra. Arrows represent changes in the peaks as temperature increases.

To aid in the evaluating the occupancy of the different CO adsorption sites as a function of desorption temperature, peak fitting was performed on each spectrum at each temperature for each material, shown in the SI in Figures S4-S7 and tables S2-S5. The results of this analysis allows us to identify the specific adsorption sites and the rate of CO desorption at each site. The results of this analysis are shown as plots of coverage versus temperature during TPD for each material in Figure 2.6. Two bridging peaks are identified for the Pd sample (labeled bridge A and B in the legend), with single bridge peaks identified for all other materials. As mentioned, with increasing temperature, the catalysts all show an increase in the hollow bound CO to Pd peak.

This peak is too small in magnitude and covers too wide of a spectrum to fit for 1:1 and 1:3 PdCu but is more pronounced and can be fit in Pd and 3:1 PdCu. In Pd and 3:1 PdCu, Figure 2.6 clearly illustrates the desorption follows a trend: First the top bound CO to Pd desorbs, followed by the desorption of the bridge bound peak. Then, we see the emergence of the peak from the CO in the hollow site. This phenomenon is consistent with the shifting of CO from top and bridge to hollow sites upon temperature-induced desorption previously reported.[36] This shift is typically attributed to the partial alleviation of CO-CO repulsion as CO desorbs.[37,38] The 1:3 PdCu shows a similar trend, but starting with the linear bound CO to Cu, followed by CO linearly bound to Pd, and then by bridging Pd.

The 1:1 PdCu appears to be an exception to this trend, showing first a sharp decrease in bridge-bound CO to Pd coverage, followed by the Pd top, and linear CO to Cu. The Cu peak follows the same trend for 1:3 and 1:1 PdCu, however.

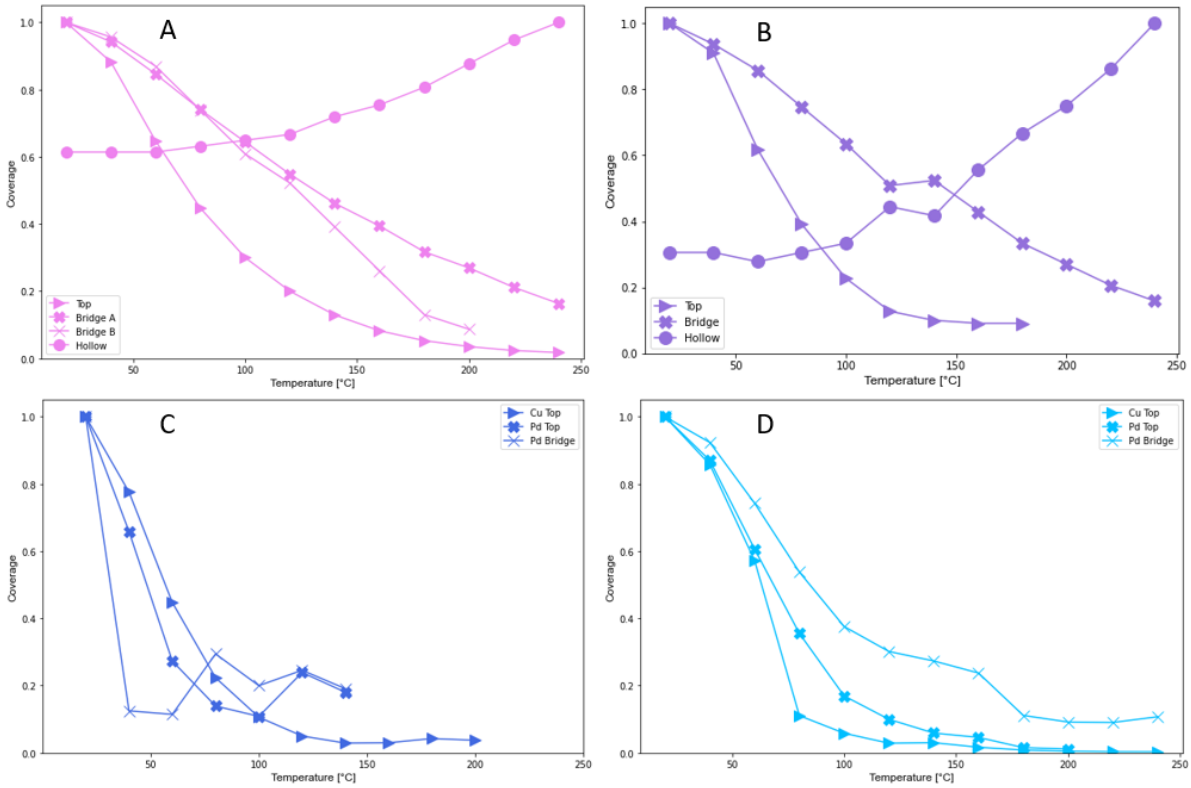

Figure 6: Coverage as a function of temperature (10 °C min^{-1} ramp) for the various CO binding configurations on Pd (A), 3:1 PdCu (B), 1:1 PdCu (C), and 1:3 PdCu (D) catalysts. Redhead's method was employed to determine coverage.

The CO DRIFTS study indicates that, under CO saturation conditions, the more active catalysts have Pd-rich surfaces, whereas less active catalysts are dominated by surface Cu coverage. This is shown by the CO on top of Cu peak present in the 1:1 and 1:3 PdCu alloys. The 3:1 PdCu sample shows no Cu-CO peak under these conditions, and displays a spectrum largely like that of the monometallic Pd. This indicates the 3:1 PdCu surface is largely dominated by Pd or that any surface Cu does not have affinity to bind with CO. The clear desorption trends from CO on-top, migrating to bridge, and then hollow sites are clear in the 3:1 PdCu and the monometallic Pd, but are not apparent in higher Cu content alloys. Conversely, the dominance of the Cu signal and lack of bound CO migration suggest the 1:1 and 1:3 PdCu alloys have much less surface Pd available than their 3:1 PdCu counterpart. The higher concentration of Cu on the surface of particles likely decreases the size and diversity of Pd surface ensembles. If surface Cu is not an active site for CO oxidation in this system this Cu dominated surface and lack of diversity and abundance of surface Pd would explain the lack of activity in 1:1 and 1:3 PdCu samples observed above.

X-ray Absorption Spectroscopy: XAS data were collected for both the "as prepared" and "post reduction" silica supported nanoparticle Pd, 3:1 PdCu, and 1:3 PdCu catalyst samples. Figure 7 displays the Pd K-edge (A, B) and Cu K-edge (C, D) XANES spectra. In Figure 7A, the Pd K-edge XANES for as prepared Pd, 3:1, and 1:3 PdCu are compared to a metallic Pd and bulk PdO. In the as prepared samples (A) the three catalyst samples all show a rising edge feature more like PdO in magnitude and shape compared to metallic Pd. Linear combination fitting (LCF) analysis was performed on the as-prepared XANES spectra to estimate the oxidic or metallic fractions represented. The results of this analysis are included in Table S12 and show that the Pd in all three catalyst is better represented by the oxide than the metal. Following reduction (Figure 2.7B) the XANES shows a shift to features in the spectra more like the Pd spectrum indictive of a transformation to metallic nanoparticles.

Figure 7C displays the Cu K-edge XANES for the as-prepared catalysts. LCF analysis (Table S12) indicates that the catalysts are comprised of 70-80% CuO with balance metallic Cu. Following reduction, the Cu in the catalyst becomes metallic (Figure 7D).

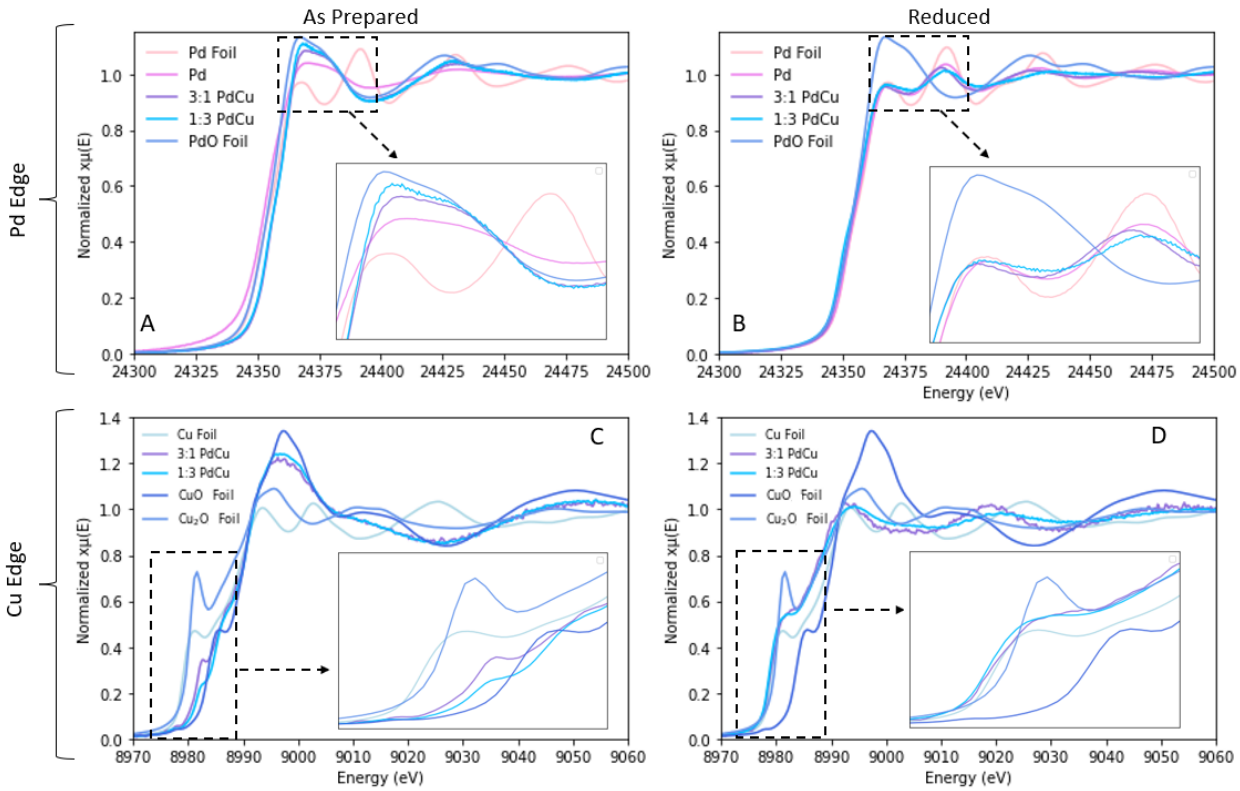

Figure 7: XANES region XAS spectra performed on as prepared, and post reduction catalyst samples. Foil XANES taking at the time of measurement included. The top panels (A and B) show Pd edge data, the bottom show Cu edge data. Panels A and C are As Prepared, B and D are Post reduction.

The results of the EXAFS modeling of the data are summarized in Tables S6 and S7, and Figures S8-S17. Figure 8 shows the resulting coordination numbers for each catalyst. The Pd-O CN for the as-prepared Pd catalyst is 1.9±0.1, which is half of normal PdO coordination. We propose this is due to a surface oxide layer, whereas the interior of the particle remains metallic.[1] In 3:1 PdCu the Pd-O CN is 3.1±0.3, and in 1:3 PdCu the CN is 3.5±0.2 in the as prepared state. This trend of increasing Pd-O CN with increasing Cu content is apparent in Figure 2.8A (pink X). However, the Pd-Pd CN also increases with increasing Cu content. It is possible the increased particle size of 1:3 PdCu compared to 3:1 PdCu (as indicated by TEM) could result in a higher overall coordination for both paths in 1:3 PdCu. The Cu in the as-prepared alloys is dominated by oxygen (Cu-O) coordination (blue X) and by a small Cu-Cu contribution (Table S12), confirming oxidation. Therefore, the as-prepared nanoparticles are dominated by oxidic bonds

opposed to metallic which agrees with the XANES analysis above.

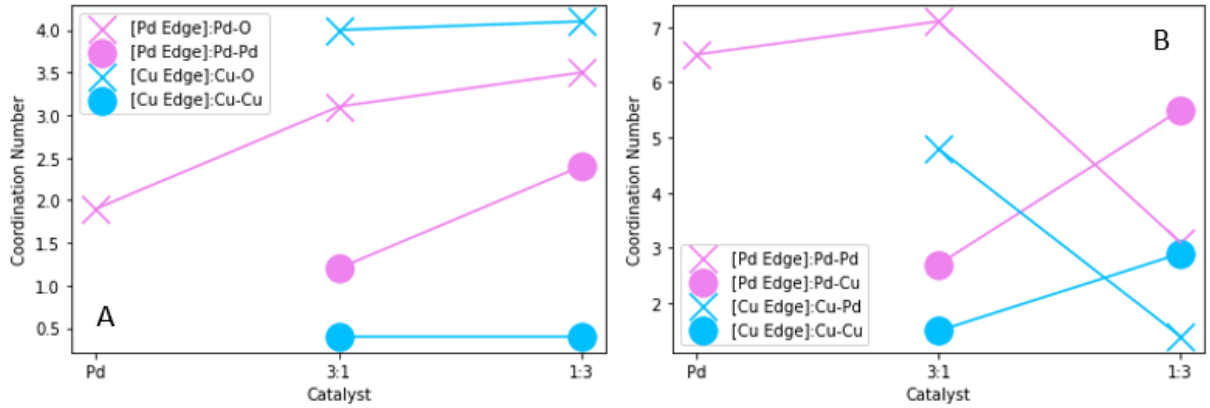

Figure 8: *Coordination environment of Cu and Pd atoms in catalysts as a function of the alloying ratio before (A) and after (B) reductive treatment.*

Following reduction (Figure 8B), the Pd-Pd CN increases between Pd and 3:1 PdCu towards a coordination of 7. In the 1:3 PdCu sample, Pd-Pd coordination is ~3, with a higher degree of Pd-Cu coordination. The 3:1 PdCu alloy has a comparatively low Pd-Cu coordination. Further, the 3:1 PdCu catalyst has little Cu-Cu coordination, whereas the 1:3 PdCu catalyst has higher Cu-Cu coordination. The 3:1 PdCu does however display more Cu-Pd coordination than the 1:3 PdCu alloy.

The differences in the Pd-Cu and Pd-Pd coordination numbers of the reduced catalysts offer indications as to the site requirements for highly active, inhibition-free catalysts. The EXAFS models of the low-activity 1:3 PdCu sample indicates that Cu is mostly surrounded by other Cu atoms, while Pd is mostly coordinated to Cu. The immediate coordination environment of the Pd atoms is enriched in Pd, while the Cu coordination environment is enriched in Cu. Given that the STEM/EDX micrographs (Figure S18) show a collocation of Pd and Cu in the microscale and previous published work [39–41]the formation of separate Cu and Pd nanoparticles is unlikely, particularly given the strong electrostatic adsorption preparation method.[19] This indicates segregation of Pd and Cu within individual nanoparticles. This observation, combined with the smaller total coordination number of Cu, compared to Pd (4.3 versus 8.6), suggests segregation of Cu to the surface of the alloy nanoparticles. This is also consistent with the DRIFTS results for the PdCu and $PdCu_3$ samples, in which mostly CO-Cu binding is observed. Furthermore, the

surface segregation of Cu in PdCu samples has been amply documented by our group and others.[39–41] .

Conversely, the highly active 3:1 PdCu sample shows considerable mixing of the Pd and the Cu. Furthermore, the total average coordination numbers on the Cu edge versus the Pd edge (6.3 versus 9.8) demonstrate that Cu is again segregated to the surface of the nanoparticles, albeit to a lesser extent, compared to the 1:3 Pd:Cu sample. Specifically, the coordination environment of Pd has 2.7±0.7 Pd-Cu bonds and 7.1±0.7 Pd-Pd bonds, while the Cu edge has 1.5±0.4 Cu-Pd bonds and 4.8±0.4 Pd-Pd bonds. These ratios are close to the nominal, suggesting mixing of the species. [42,43]

4. Conclusions

We have synthesized different atomic ratio of Pd and Cu in PdCu alloyed nanoparticles in catalysts as a lever to control the structure and, through this structure tuning, their activity for CO oxidation activity and the CO-surface interactions on these alloys., The results of this work inform that there is an optimal Cu incorporation, corresponding to a 3:1 molar ratio of Pd:Cu. At this level, CO oxidation takes place at low temperature and without inhibition by NO. Conversely, monometallic Pd samples are highly active, but are also inhibited by NO, while Cu-rich samples show both lower activity and inhibition. A combination of DRIFTS and XAS studies indicate that, at higher Cu alloying ratios, the Cu covers the active surface of the Pd, leading to weak CO adsorption onto the surface. Conversely, fractional Cu incorporation at lower ratios offers a more diverse surface in terms of CO, NO, and oxygen binding.

5. Acknowledgements

S.K. was supported by the DOE BES, Office of Workforce Development for Teachers and Scientists, Office of Science Graduate Student Research (SCGSR) program, which is administered by the Oak Ridge Institute for Science and Education for the DOE under contract number DE-SC0014664.This research used resources of the Stanford Synchrotron Radiation Lightsource. Use of the Stanford Synchrotron Radiation Lightsource, SLAC National Accelerator Laboratory, is supported by the U.S. Department of Energy, Office of Science, Office of Basic Energy Sciences under Contract No. DE-AC02-76SF00515. Co-ACCESS, part of the SUNCAT Center for Interface Science and Catalysis, is supported by the U.S. Department of Energy, Office of Basic Energy Sciences, Chemical Sciences, Geosciences and Biosciences

Division. Portions of this work were supported by the National Science Foundation under Grant No. 2310361.

6. Conflicts of Interest

Konstantinos A. Goulas is co-inventor in a patent describing the invention of PdCu catalysts for diesel oxidation catalysis (WO2021163294A1).

7. References

(1) Johnson, T.; Joshi, A. Review of Vehicle Engine Efficiency and Emissions. *SAE Int. J. Engines* **2018**, *11* (6), 1307–1330. https://doi.org/10.4271/2018-01-0329.

(2) Yu, T.; Li, K.; Wu, Q.; Yao, P.; Ke, J.; Wang, B.; Wang, Y. Diesel Engine Emission Aftertreatment Device Aging Mechanism and Durability Assessment Methods: A Review. *Atmosphere (Basel).* **2023**, *14* (2). https://doi.org/10.3390/ATMOS14020314.

(3) Crosignani, P.; Nanni, A.; Pepe, N.; Pozzi, C.; Silibello, C.; Poggio, A.; Conte, M. The Effect of Non-Compliance of Diesel Vehicle Emissions with Euro Limits on Mortality in the City of Milan. *Atmos. 2021, Vol. 12, Page 342* **2021**, *12* (3), 342. https://doi.org/10.3390/ATMOS12030342.

(4) Apicella, B.; Mancaruso, E.; Russo, C.; Tregrossi, A.; Oliano, M. M.; Ciajolo, A.; Vaglieco, B. M. Effect of After-Treatment Systems on Particulate Matter Emissions in Diesel Engine Exhaust. *Exp. Therm. Fluid Sci.* **2020**, *116*, 110107. https://doi.org/10.1016/J.EXPTHERMFLUSCI.2020.110107.

(5) Rahman, S. M. A.; Rizwanul Fattah, I. M.; Ong, H. C.; Zamri, M. F. M. A. State-of-the-Art of Strategies to Reduce Exhaust Emissions from Diesel Engine Vehicles. *Energies 2021, Vol. 14, Page 1766* **2021**, *14* (6), 1766. https://doi.org/10.3390/EN14061766.

(6) Rappé, K. G.; DiMaggio, C.; Pihl, J. A.; Theis, J. R.; Oh, S. H.; Fisher, G. B.; Parks, J.; Easterling, V. G.; Yang, M.; Stewart, M. L.; Howden, K. C. Aftertreatment Protocols for Catalyst Characterization and Performance Evaluation: Low-Temperature Oxidation, Storage, Three-Way, and NH 3 -SCR Catalyst Test Protocols. *Emiss. Control Sci. Technol.* **2019**, *5* (2), 183–214. https://doi.org/10.1007/S40825-019-00120-7/METRICS.

(7) Wong, A. P.; Kyriakidou, E. A.; Toops, T. J.; Regalbuto, J. R. The Catalytic Behavior of Precisely Synthesized Pt-Pd Bimetallic Catalysts for Use as Diesel Oxidation Catalysts. *Catal. Today* **2016**, *267*, 145–156. https://doi.org/10.1016/j.cattod.2016.02.011.

(8) Kim, M.-Y.; Kyriakidou, E. A.; Choi, J.-S.; Toops, T. J.; Binder, A. J.; Thomas, C.; Parks, J. E.; Schwartz, V.; Chen, J.; Hensley, D. K. Enhancing Low-Temperature Activity and Durability of Pd-Based Diesel Oxidation Catalysts Using ZrO2 Supports. *Appl. Catal. B Environ.* **2016**, *187*, 181–194. https://doi.org/10.1016/J.APCATB.2016.01.023.

(9) Wang, C.; Binder, A. J.; Toops, T. J.; Lauterbach, J.; Sasmaz, E. Evaluation of Mn and Sn-Modified Pd-Ce-Based Catalysts for Low-Temperature Diesel Exhaust Oxidation. *Emiss. Control Sci. Technol.* **2017**, *3* (1), 37–46. https://doi.org/10.1007/S40825-016-

0056-9/METRICS.

(10) Liu, C. H.; Chen, J.; Toops, T. J.; Choi, J. S.; Thomas, C.; Lance, M. J.; Kyriakidou, E. A. Hydrothermally Stable Pd/SiO2@Zr Core@Shell Catalysts for Diesel Oxidation Applications. *Chem. Eng. J.* **2021**, *425*, 130637. https://doi.org/10.1016/J.CEJ.2021.130637.

(11) Liu, C. H.; Porter, S.; Chen, J.; Pham, H.; Peterson, E. J.; Khatri, P.; Toops, T. J.; Datye, A.; Kyriakidou, E. A. Enhanced Low Temperature Performance of Bimetallic Pd/Pt/SiO2(Core)@Zr(Shell) Diesel Oxidation Catalysts. *Appl. Catal. B Environ.* **2023**, *327*, 122436. https://doi.org/10.1016/J.APCATB.2023.122436.

(12) Březina, J.; Pečinka, R.; Boutikos, P.; Kočí, P. Comparison of Dual CO Light-off Effect on Pt/CeO2/γ-Al2O3, Pd/CeO2/γ-Al2O3, Pt/γ-Al2O3 and Pd/γ-Al2O3 in the Presence of C3H6. *Chem. Eng. Sci.* **2020**, *218*, 115542. https://doi.org/10.1016/J.CES.2020.115542.

(13) Boutikos, P.; Březina, J.; Buzková Arvajová, A.; Kočí, P. Comparison of O2 and NO2 Impact on PtOx and PdOx Formation in Diesel Oxidation Catalysts and Their Reduction by CO and C3H6 Pulses. *Chem. Eng. J.* **2019**, *377*, 119654. https://doi.org/10.1016/J.CEJ.2018.08.040.

(14) Hazlett, M. J.; Epling, W. S. Spatially Resolving CO and C3H6 Oxidation Reactions in a Pt/Al2O3 Model Oxidation Catalyst. *Catal. Today* **2016**, *267*, 157–166. https://doi.org/10.1016/j.cattod.2015.11.033.

(15) Prikhodko, V. Y.; Curran, S. J.; Parks, J. E.; Wagner, R. M. Effectiveness of Diesel Oxidation Catalyst in Reducing HC and CO Emissions from Reactivity Controlled Compression Ignition. *SAE Int. J. Fuels Lubr.* **2013**, *6* (2), 329–335. https://doi.org/10.4271/2013-01-0515.

(16) Song, Y.; Grabow, L. C. Activity Trends for Catalytic CO and NO Co-Oxidation at Low Temperature Diesel Emission Conditions. *Ind. Eng. Chem. Res.* **2018**, acs.iecr.8b01905. https://doi.org/10.1021/acs.iecr.8b01905.

(17) Kristy, S.; Svadlenak, S.; Hoffman, A. S.; Bare, S. R.; Goulas, K. A. Spectroscopic Determination of Metal Redox and Segregation Effects during CO and CO/NO Oxidation over Silica-Supported Pd and PdCu Catalysts. *Appl. Catal. B Environ.* **2024**, *342*, 123329. https://doi.org/10.1016/J.APCATB.2023.123329.

(18) Song, Y.; Svadlenak, S.; Bathena, T.; Hazlett, M. J.; Epling, W. S.; Goulas, K. A.; Grabow, L. C. PdCu Alloy Catalyst for Inhibition-Free, Low-Temperature CO Oxidation. *ChemCatChem* **2024**, *16* (1), e202301024. https://doi.org/10.1002/CCTC.202301024.

(19) Wong, A.; Liu, Q.; Griffin, S.; Nicholls, A.; Regalbuto, J. R. Synthesis of Ultrasmall, Homogeneously Alloyed, Bimetallic Nanoparticles on Silica Supports. *Science (80-.).* **2017**, *358* (6369), 1427–1430. https://doi.org/10.1126/SCIENCE.AAO6538/SUPPL_FILE/AAO6538_WONG_SM.PDF.

(20) Jiao, L.; Regalbuto, J. R. The Synthesis of Highly Dispersed Noble and Base Metals on Silica via Strong Electrostatic Adsorption: II. Mesoporous Silica SBA-15. *J. Catal.* **2008**, *260* (2), 342–350. https://doi.org/10.1016/J.JCAT.2008.09.023.

(21) Jiao, L.; Regalbuto, J. R. The Synthesis of Highly Dispersed Noble and Base Metals on Silica via Strong Electrostatic Adsorption: I. Amorphous Silica. *J. Catal.* **2008**, *260* (2), 329–341. https://doi.org/10.1016/J.JCAT.2008.09.022.

(22) Cho, H. R.; Regalbuto, J. R. The Rational Synthesis of Pt-Pd Bimetallic Catalysts by Electrostatic Adsorption. *Catal. Today* **2015**, *246*, 143–153. https://doi.org/10.1016/J.CATTOD.2014.09.029.

(23) Masel, R. I. Principles of Adsorption and Reaction on Solid Surfaces. 804.

(24) Hoffman, A. S.; Singh, J. A.; Bent, S. F.; Bare, S. R. In Situ Observation of Phase Changes of a Silica-Supported Cobalt Catalyst for the Fischerâ€“Tropsch Process by the Development of a Synchrotron-Compatible InÂ Situ/Operando Powder X-Ray Diffraction Cell. *J. Synchrotron Radiat.* **2018**, *25* (6), 1673–1682. https://doi.org/10.1107/S1600577518013942/FV5092SUP1.PDF.

(25) Goulas, K. A.; Lee, J. D.; Zheng, W.; Lym, J.; Yao, S.; Oh, D. S.; Wang, C.; Gorte, R. J.; Chen, J. G.; Murray, C. B.; Vlachos, D. G. Spectroscopic Characterization of a Highly Selective NiCu3/C Hydrodeoxygenation Catalyst. *Catal. Sci. Technol.* **2018**, *8* (23), 6100–6108. https://doi.org/10.1039/c8cy01280f.

(26) Ravel, B.; Newville, M. ATHENA, ARTEMIS, HEPHAESTUS: Data Analysis for X-Ray Absorption Spectroscopy Using IFEFFIT. *urn:issn:0909-0495* **2005**, *12* (4), 537–541. https://doi.org/10.1107/S0909049505012719.

(27) Jain, A.; Ong, S. P.; Hautier, G.; Chen, W.; Richards, W. D.; Dacek, S.; Cholia, S.; Gunter, D.; Skinner, D.; Ceder, G.; Persson, K. A. Commentary: The Materials Project: A Materials Genome Approach to Accelerating Materials Innovation. *APL Mater.* **2013**, *1* (1). https://doi.org/10.1063/1.4812323/119685.

(28) Mc Grane, L.; Douglas, R.; Irwin, K.; Stewart, J.; Woods, A.; Muehlstaedt, F. A Study of the Effect of Light-Off Temperatures and Light-Off Curve Shape on the Cumulative Emissions Performance of 3-Way Catalytic Converters. *SAE Tech. Pap.* **2021**, No. 2021. https://doi.org/10.4271/2021-01-0594.

(29) Stewart, J.; Douglas, R.; Goguet, A.; Stere, C. E.; Blades, L. A Mathematical Approach to the Balancing of Mass Transfer and Reaction Kinetics in Dual Kinetic Model for Automotive Catalysis. *SAE Tech. Pap.* **2014**, *2014-October*. https://doi.org/10.4271/2014-01-2821.

(30) Kim, D. H.; Kung, M. C.; Kozlova, A.; Yuan, S. D.; Kung, H. H. Synergism between Pt/Al 2O 3 and Au/TiO 2 in the Low Temperature Oxidation of Propene. *Catal. Letters* **2004**, *98* (1), 11–15. https://doi.org/10.1007/S10562-004-6440-Z/METRICS.

(31) Jiaqiang, E.; Luo, J.; Han, D.; Tan, Y.; Feng, C.; Deng, Y. Effects of Different Catalysts on Light-off Temperature of Volatile Organic Components in the Rotary Diesel Particulate Filter during the Regeneration. *Fuel* **2022**, *310*, 122451. https://doi.org/10.1016/J.FUEL.2021.122451.

(32) Al-Adwani, S. M.; Soares, J.; Epling, W. S. Evaluating the Effects of Precious Metal Distribution along a Monolith-Supported Catalyst for CO Oxidation. *Ind. Eng. Chem. Res.*

2012, *51* (19), 6672–6679. https://doi.org/10.1021/IE202969U.

(33) Ball, M. R.; Rivera-Dones, K. R.; Gilcher, E. B.; Ausman, S. F.; Hullfish, C. W.; Lebrón, E. A.; Dumesic, J. A. AgPd and CuPd Catalysts for Selective Hydrogenation of Acetylene. *ACS Catal.* **2020**, *10* (15), 8567–8581. https://doi.org/10.1021/acscatal.0c01536.

(34) Bertarione, S.; Scarano, D.; Zecchina, A.; Johánek, V.; Hoffmann, J.; Schauermann, S.; Frank, M. M.; Libuda, J.; Rupprechter, G.; Freund, H. J. Surface Reactivity of Pd Nanoparticles Supported on Polycrystalline Substrates As Compared to Thin Film Model Catalysts: Infrared Study of CO Adsorption. *J. Phys. Chem. B* **2004**, *108* (11), 3603–3613. https://doi.org/10.1021/JP036718T.

(35) Hoffman, A. S.; Fang, C. Y.; Gates, B. C. Homogeneity of Surface Sites in Supported Single-Site Metal Catalysts: Assessment with Band Widths of Metal Carbonyl Infrared Spectra. *J. Phys. Chem. Lett.* **2016**, *7* (19), 3854–3860. https://doi.org/10.1021/ACS.JPCLETT.6B01825/ASSET/IMAGES/LARGE/JZ-2016-018254_0004.JPEG.

(36) Ozensoy, E.; Goodman, D. W. Vibrational Spectroscopic Studies on CO Adsorption, NO Adsorption CO + NO Reaction on Pd Model Catalysts. *Phys. Chem. Chem. Phys.* **2004**, *6* (14), 3765–3778. https://doi.org/10.1039/B402302A.

(37) Daniell, W.; Landes, H.; Fouad, N. E.; Knözinger, H. Influence of Pretreatment Atmosphere on the Nature of Silica-Supported Pd Generated via Decomposition of Pd(Acac)2: An FTIR Spectroscopic Study of Adsorbed CO. *J. Mol. Catal. A Chem.* **2002**, *178* (1–2), 211–218. https://doi.org/10.1016/S1381-1169(01)00323-5.

(38) Rainer, D. R.; Wu, M. -C.; Mahon, D. I.; Goodman, D. W. Adsorption of CO on Pd/Al2O3/Ta(110) Model Catalysts. *J. Vac. Sci. Technol. A Vacuum, Surfaces, Film.* **1998**, *14* (3), 1184. https://doi.org/10.1116/1.580263.

(39) Olekszyszen, D. N.; Albuquerque, B. L.; Silva, D. D. O.; Tripodi, G. L.; De Oliveira, D. C.; Domingos, J. B. Core–Shell PdCu Bimetallic Colloidal Nanoparticles in Sonogashira Cross-Coupling Reaction: Mechanistic Insights into the Catalyst Mode of Action. *Nanoscale* **2020**, *12* (2), 1171–1179. https://doi.org/10.1039/C9NR09075D.

(40) Goulas, K. A.; Song, Y.; Johnson, G. R.; Chen, J. P.; Gokhale, A. A.; Grabow, L. C.; Toste, F. D. Selectivity Tuning over Monometallic and Bimetallic Dehydrogenation Catalysts: Effects of Support and Particle Size. *Catal. Sci. Technol.* **2018**, *8* (1). https://doi.org/10.1039/c7cy01306j.

(41) Pasquale, L.; Najafishirtari, S.; Brescia, R.; Scarpellini, A.; Demirci, C.; Colombo, M.; Manna, L. Atmosphere-Induced Transient Structural Transformations of Pd-Cu and Pt-Cu Alloy Nanocrystals. *Chem. Mater.* **2021**, *33* (22), 8635–8648. https://doi.org/10.1021/ACS.CHEMMATER.1C02377/ASSET/IMAGES/LARGE/CM1C02377_0007.JPEG.

(42) McGuire, S. C.; Ebrahim, A. M.; Hurley, N.; Zhang, L.; Frenkel, A. I.; Wong, S. S. Reconciling Structure Prediction of Alloyed, Ultrathin Nanowires with Spectroscopy. *Chem. Sci.* **2021**, *12* (20), 7158–7173. https://doi.org/10.1039/D1SC00627D.

(43) Lawrence, R. L.; Olagunju, M. O.; Liu, Y.; Mahalingam, K.; Slocik, J. M.; Naik, R. R.; Frenkel, A. I.; Knecht, M. R. Remote Controlled Optical Manipulation of Bimetallic Nanoparticle Catalysts Using Peptides. *Catal. Sci. Technol.* **2021**, *11* (7), 2386–2395. https://doi.org/10.1039/D1CY00189B.